Intelligent Complementary Terminal Sliding Mode Using Multiloop Neural Network for Active Power Filter

Lei Zhang and Juntao Fei, *Senior Member, IEEE*

***Abstract*—This article presents a new intelligent sliding-mode control approach to effectively achieve harmonic suppression of an active power filter (APF). An intelligent complementary terminal sliding-mode controller is proposed to improve the control accuracy of current loop and deal with the lumped disturbances in the system. Complementary terminal sliding-mode control combines the features of complementary sliding-mode control and terminal sliding-mode control and does not depend on the accurate dynamic model. In addition, in order to reduce chattering, a multiloop neural network (MLNN), whose parameter learning laws of MLNN are derived based on the Lyapunov laws, is proposed to approximate the unknown nonlinear function term in the APF dynamic model, thus reducing the burden of sliding-mode control. Finally, within the computing power of control board, the detailed simulation and hardware experiments are carried out to demonstrate better harmonic suppression, and steady-state and dynamic performance compared with the existing methods.**

***Index Terms*—Active power filter (APF), complementary sliding-mode control (CSMC), multiloop neural network (MLNN), terminal sliding-mode control (TSMC).**

I. Introduction

With the development of modern industry, power electronic technology has been involved in all aspects of human life, and the updated speed of power electronic equipment is also faster and faster. However, due to the increase of nonlinear equipment in the power system, harmonic pollution is becoming increasingly serious [1], [2]. Therefore, various methods of harmonic suppression in the power grid have become a research hotspot in recent years. The common method of harmonic suppression is to install filtering devices in the power system to filter out harmonics. Common power filters can be divided into passive power filters (PPFs) and active power filters (APFs). However, PPF cannot compensate for harmonics and reactive power quickly and dynamically [3]. On the contrary, APF can quickly track the changing harmonic current in the power grid, and its compensation performance is not affected by the frequency fluctuation of the power grid [4]. Therefore, the application of APF is more and more extensive in real life.

Some control methods for the APF current loop have been proposed in the existing literature. In [5], a nonlinear unified control strategy via feedback linearization was proposed for an APF to suppress low-frequency harmonics and convert the voltage and current dual-loop control into energy single-loop control. In [6], a fractional-order repetitive control method with a fixed sampling rate was proposed to improve the shortcomings of the traditional repetitive control that cannot accurately compensate for variable-frequency periodic signals. In order to improve the compensation performance of the APF, a vector proportional-integral (PI) current control method using a phase-locked loop to update the gain was proposed in [7]. However, the above methods have high requirements on the accuracy of the dynamic model of the APF, which is difficult to achieve in practical applications. Therefore, other advanced control methods need to be used to overcome this difficulty.

Since the advantage of sliding-mode control (SMC) is robustness to external disturbances as well as changes and uncertainties of internal parameters, it is very suitable for APF current control, which is difficult to model and requires high control accuracy [8], [9]. However, SMC has a chattering problem. Therefore, over the years, some sliding-mode controllers have been proposed to improve their performance, such as supertwisting SMC [10], [11], adaptive SMC (ASMC) [12], [13], fuzzy integral SMC [14], and complementary SMC (CSMC) [15]. Among them, CSMC can not only reduce chattering but also improve tracking accuracy [16]. With CSMC method, the tracking error can be shown to be 50% less than that of ordinary SMC using saturation function [17], [18], [19]. In [17], a novel disturbance-observer-based CSMC speed controller was proposed to improve the speed control accuracy of permanent magnet synchronous motors. In [18], an adaptive CSMC with a d-axis current control scheme was designed for the speed regulation of a synchronous reluctance motor. In [19], CSMC method was utilized to improve the performance of permanent magnet linear synchronous motor and a radial-basis function network was introduced to estimate the lumped uncertainty.

Manuscript received 9 December 2022; revised 26 January 2023 and 3 March 2023; accepted 10 April 2023. Date of publication 13 April 2023; date of current version 21 June 2023. This work was supported by the National Science Foundation of China under Grant 62273131. Recommended for publication by Associate Editor B. Singh. *(Corresponding author: Juntao Fei.)*

The authors are with the College of IoT Engineering, Jiangsu Key Laboratory of Power Transmission and Distribution Equipment Technology, Hohai University, Changzhou 213022, China. (e-mail: jtfei@yahoo.com).

Color versions of one or more figures in this article are available at https://doi.org/10.1109/TPEL.2023.3266738.

Digital Object Identifier 10.1109/TPEL.2023.3266738

However, SMC cannot ensure that the tracking error converges to zero in a finite time after the system state reaches the sliding-mode surface. Therefore, terminal sliding-mode control (TSMC) is proposed to make the sliding-mode surface and tracking error converge to zero in finite time [20], [21], [22]. Thus, in this article, a complementary terminal sliding-mode controller (CTSMC) method that combines the advantages of TSMC and CSMC is proposed and can ensure finite-time convergence.

In addition, the combination of the SMC method and various observers [23], [24], [25] or neural networks (NNs) has also been the focus of research in recent years. Due to the strong learning ability of NN, it can approximate any nonlinear function theoretically. Especially, recurrent neural network (RNN) can combine the output signal of the previous moment and the input of the NN, improve the learning ability, and prevent the output mutation in the presence of external parameter changes [26]. A new fully connected RNN containing the structure of internal feedback loop and external feedback loop was designed in [27], and all hidden layer neurons receive the signal from other hidden layer neurons and output layer. Self-constructing fuzzy neural sliding-mode controller is investigated to greatly enhance the structure and approximation capability of NN [38], [39], [40].

Motivated by the pieces of literature above, a complementary terminal sliding-mode controller using multiloop neural network (CTSMC-MLNN) with a CTSMC that combines the advantages of TSMC and CSMC and an MLNN that contains two recurrent loops to estimate unknown nonlinear function is proposed in this article. The MLNN can store the output information of the neurons and the whole NN at the first two moments, which enhances the approximation ability of the nonlinear function of the NN and does not increase the computational cost too much. The contribution of this article can be concluded as follows.

1) A novel SMC method combining CSMC and TSMC is proposed in this article. It not only has the characteristics of small tracking errors and reduced chattering but also ensures that the tracking error converges in a finite time.
2) An MLNN with a simple structure and combining the advantages of internal feedback NN and external feedback NN is used to approximate the unknown nonlinear function in the dynamic model of APF. All parameters in MLNN can automatically converge to the optimal values. Therefore, the burden of the SMC to suppress total disturbance is reduced, and chattering is further weakened.
3) The CTSMC-MLNN control scheme has been implemented in the hardware platform based on dSPACE 1104 successfully. Meanwhile, the superiority of the proposed control scheme was verified through detailed comparisons and analysis.

The rest of this article is organized as follows. In Section II, a second-order dynamic model of APF is established. In Section III, a new CTSMC method is proposed and analyzed. In Section IV, a new intelligent SMC strategy is designed and its stability is proved. Simulation study and hardware experimental results are given in Section V and Section VI, respectively. Finally, Section VII concludes this article.

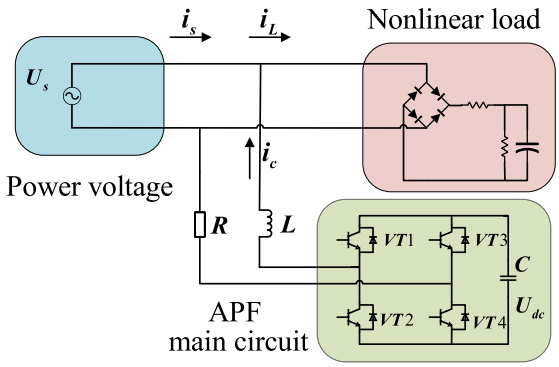

Fig. 1. Circuit model of SAPF.

II. Modeling of APF

APF can be classified into single-phase APF (SAPF), three-phase three-wire, and three-phase four-wire APF according to the number of phases. SAPF is mainly used in low-power applications, such as residential areas, schools, and office buildings. Therefore, with the economic development and population growth, SAPF has a broad application prospect.

The circuit model of a typical SAPF is shown in Fig. 1 and mainly includes three components: grid voltage, nonlinear load, and APF main circuit. The core devices of the APF main circuit are insulated gate bipolar transistiors (IGBTs), which are a kind of switching devices with high voltage resistance and fast switching frequency. Besides, the nonlinear load is acted by an uncontrollable rectifier bridge with capacitive load. An ac power supply with the amplitude of 24 V with the frequency of 50 Hz is chosen to simulate the actual grid voltage operation. The principle of APF filtering out harmonics is to offset the harmonic current generated by the nonlinear load connected to the circuit by outputting the compensation current.

According to Fig. 1, the dynamic model of an SAPF can be given in the following part. According to Kirchhoff's voltage and current laws, the circuit equation is written as follows:

$$\dot{i}_c = -\frac{R}{L} i_c + \frac{1}{L} U_s - \frac{1}{L} U \cdot U_{\mathrm{dc}} \tag{1}$$

where i_c is a compensation current, U_s is a grid voltage, i_L is a load current, U_{dc} is the voltage of the dc-side capacitor, U is the duty cycle of IGBT, and L and R are the nominal values of the inductance and resistance of ac side, respectively.

The derivative of (1) can be derived as follows:

$$\ddot{i}_c = \frac{R^2}{L^2} i_c - \frac{R}{L^2} U_s + \frac{1}{L} \dot{U}_s + \left(\frac{R}{L^2} U_{\mathrm{dc}} - \frac{1}{L} \dot{U}_{\mathrm{dc}} \right) \cdot U. \tag{2}$$

Therefore, the second-order mathematical model of APF can be obtained as follows:

$$\ddot{x} = f(x) + bu + d(t) \tag{3}$$

where x represents the compensation current i_c, $d(t)$ is a lumped disturbance, which includes external disturbance, parameter perturbation, and unmodeled part. We supposed that $d(t)$ is continuous and differentiable bounded, which satisfies $|d(t)| \leq D$,

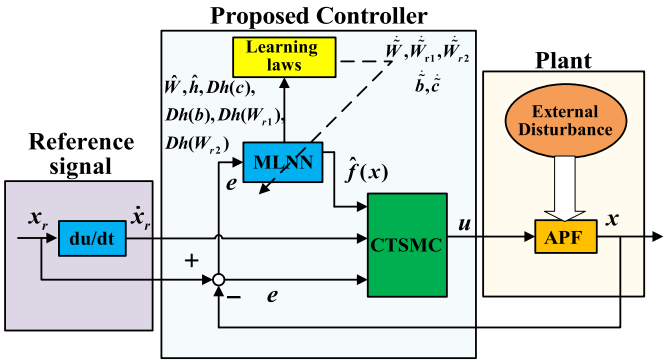

Fig. 2. Block diagram of the proposed control system.

where D is a positive constant. The expressions for $f(x)$ and b are expressed as follows:

$$f(x) = \frac{R^2}{L^2} i_c - \frac{R}{L^2} U_s + \frac{1}{L} U_s \tag{4}$$

$$b = \frac{R}{L^2} U_{\rm dc} - \frac{1}{L} \dot{U}_{\rm dc}. \tag{5}$$

In Section III, a CTSMC-MLNN will be designed for the APF model (3).

III. Controller Design

The block diagram of the proposed control system for APF is shown in Fig. 2. The control goal is to design a control system to achieve the aim that the compensation current i_c tracks the reference current i_r obtained by the harmonic detection algorithm. The signal x_r in Fig. 2 represents the reference current.

Define the tracking error

$$e = x - x_r. \tag{6}$$

Then, its derivative and its second derivative are as follows:

$$\dot{e} = \dot{x} - \dot{x}_r \tag{7}$$

$$\ddot{e} = \ddot{x} - \ddot{x}_r. \tag{8}$$

Substituting (3) into (8) obtains

$$\ddot{e} = \ddot{x} - \ddot{x}_r = f(x) + bu + d(t) - \ddot{x}_r. \tag{9}$$

Then, the generalized sliding-mode surface is defined as follows:

$$S_g = \dot{e} + \lambda e^m + 2\lambda e + \lambda^2 \int_0^t (e^m + e) d\tau \tag{10}$$

where λ is a positive constant, $m = \frac{q}{p} < 1$, $p > 0$, and $q > 0$.

Furthermore, a complementary sliding-mode surface can be designed as follows:

$$S_c = \dot{e} + \lambda e^m - \lambda^2 \int_0^t (e^m + e) d\tau. \tag{11}$$

Taking the derivative of (10) and (11) yields

$$\dot{S}_g = \ddot{e} + 2\lambda \dot{e} + \lambda m e^{m-1} \dot{e} + \lambda^2 (e^m + e) \tag{12}$$

$$\dot{S}_c = \ddot{e} + \lambda m e^{m-1} \dot{e} - \lambda^2 (e^m + e). \tag{13}$$

An important result can be obtained from (12) and (13) as follows:

$$\dot{S}_c - \dot{S}_g = \lambda (S_c + S_g). \tag{14}$$

Thus, an equivalent control law is derived as follows:

$$u_{\rm eq} = -\frac{1}{b} [f(x) - \ddot{x}_r + \lambda (2\dot{e} + m e^{m-1} \dot{e} + \lambda e^m + \lambda e) + \lambda s_c]. \tag{15}$$

The switching control law is designed as follows:

$$u_{\rm sw} = -\frac{1}{b} K_w {\rm sat} \left(\frac{S_g + S_c}{\phi} \right). \tag{16}$$

Thus, the final controller is obtained as follows:

$$u = u_{\rm eq} + u_{\rm sw} \tag{17}$$

where K_w is a positive constant and ${\rm sat}(\cdot)$ is a saturation function whose expression is defined as follows:

$${\rm sat} \left(\frac{S_g + S_c}{\phi} \right) = \begin{cases} 1, & S_g + S_c \geq \phi \\ \frac{S_g + S_c}{\phi}, & -\phi < S_g + S_c < \phi \\ -1, & S_g + S_c \leq \phi \end{cases} \tag{18}$$

where ϕ represents a boundary-layer thickness.

Theorem1: If the sliding-mode switching term gain K_w satisfies $K_w \geq D$, it can be ensured that the tracking error trajectory will reach the boundary layer: $|S_g + S_c| \leq \phi$ in finite time.

Proof: A Lyapunov function is chosen as follows:

$$V_1 = \frac{1}{2} (S_g^2 + S_c^2). \tag{19}$$

Taking the time derivative of (19) and using (12)–(17) obtain

$$\begin{aligned} \dot{V}_1 &= S_g \dot{S}_g + S_c \dot{S}_c = (S_g + S_c)(\dot{S}_g - \lambda S_c) \\ &= (S_g + S_c)[\ddot{e} + 2\lambda \dot{e} + \lambda^2 (e^m + e) + \lambda m e^{m-1} \dot{e}] \\ &= \dot{V}_1 = (S_g + S_c)[f(x) + bu + d(t) - \ddot{x}_r + 2\lambda \dot{e} \\ &\quad + \lambda^2 (e^m + e) + \lambda m e^{m-1} \dot{e}] \\ &= (S_g + S_c)[-K_w {\rm sat}(S_g + S_c) + d(t) - \lambda S_g - \lambda S_c] \\ &\leq -\lambda (S_g + S_c)^2 - K_w |S_g + S_c| + |S_g + S_c| \, |d(t)| \\ &= -\lambda (S_g + S_c)^2 + (-K_w + |d(t)|) |S_g + S_c| \, . \end{aligned} \tag{20}$$

Thus, the $\dot{V}_1 \leq 0$ is ensured when $|S_g + S_c| \geq \phi$. This ensures that any position-error trajectory will reach the boundary layer $|S_g + S_c| \leq \phi$ in finite time.

Remark 1: After all error tracking trajectories outside the boundary layer converge to the boundary layer, then they slide to the zero field along the intersection of the two sliding-mode surfaces, i.e., $(S_g = S_c = 0)$. Therefore, the stability of the CTSMC system can be guaranteed and the tracking error converges to the closed domain in a finite time [19].

However, due to the uncertainty of modeling, the above SMC method needs to select a large switching gain to offset the lumped disturbance. Therefore, considering the simplicity of the structure and the approximation ability, an MLNN is selected in this article for mimicking the nonlinear function $f(x)$ to reduce the burden of SMC in Section IV.

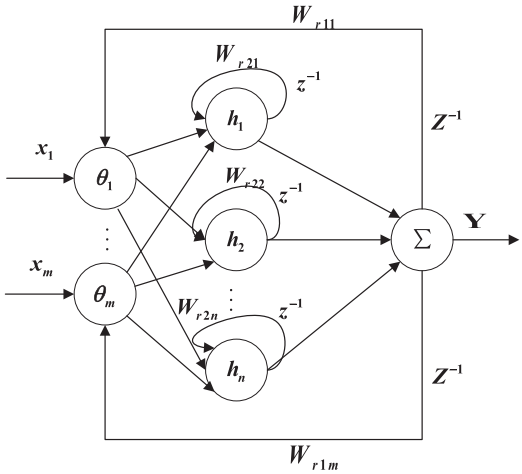

Fig. 3. Structure of MLNN.

IV. Multiloop RNN

A. Structure of MLNN

It is well known that radial basis function NN (RBFNN) is often used as a function approximator because it has characteristics similar to fuzzy systems and fast convergence speed. Therefore, in order to further improve the approximation ability of the NN, MLNN with internal feedback and external feedback structure is used in this article. The architecture of the MLNN, as shown in Fig. 3, has three layers, including input layer, hidden layer, and output layer.

1) *Input Layer*: It receives the input signal and feedback signal from the output layer. For every node $i = 1, \ldots, m$; the node input and node output are designed as follows:

$$\theta_i = \begin{cases} \frac{W_{r1i} x_i \text{ex}Y}{\text{exex}Y} & \text{if exex}Y \neq 0 \\ W_{r1i} x_i & \text{if exex}Y = 0 \end{cases} \tag{21}$$

where x_i and θ_i are the input signal and output of the ith node, respectively. ex$Y$ is the output signal of the output layer calculated in the last moment, and exex$Y$ is the output signal of the output layer in the moment before ex$Y$. W_{r1i} is the weight of the external feedback loop.

2) *Hidden Layer:* Every node in this layer receives an input signal that includes output signals of the input layer and the internal feedback link at the last moment. In this layer, the output signal of every node $j = 1, \ldots, n$ is expressed as follows:

$$h_j = e^{-\text{net}_j}, \quad \text{net}_j = \sum_{j=1}^{m} \frac{(\theta_i + W_{r2j} \text{exh}_j - c_{ij})^2}{b_{ij}^2} \tag{22}$$

where θ_i is the input signal of the ith node in the input layer. W_{r2j} is the weight of the internal feedback loop and exh_j is the output signal of the jth hidden layer node at the last moment. Besides, c_{ij} and b_{ij} are the mean value and the standard deviation of the Gaussian function in the jth node for the ith input node.

3) *Output layer:* The output in the output layer is the summation of the hidden layer outputs multiplied by the corresponding weights, given in the form

$$Y = \sum_{j=1}^{n} W_j h_j. \tag{23}$$

where W_j is the weight connecting the jth node in the hidden layer with the output node. Y represents the final output of this NN.

Arranging all the parameters of the NN in the form of vectors as (24)–(28)

$$W = \begin{bmatrix} W_1, & W_2, \ldots, & W_n \end{bmatrix} \in \Re^n \tag{24}$$

$$W_{r1} = [W_{r11}, W_{r12}, \ldots, W_{r1m}] \in \Re^m \tag{25}$$

$$W_{r2} = [W_{r21}, W_{r22}, \ldots, W_{r2n}] \in \Re^n \tag{26}$$

$$C = \begin{bmatrix} c_{11} & \ldots & c_{m1} & , c_{12} \ldots c_{m2}, \ldots, c_{1n} \ldots c_{mn} \end{bmatrix}^T \in \Re^{m \cdot n} \tag{27}$$

$$B = \begin{bmatrix} b_{11} & \ldots & b_{m1}, b_{12} \ldots b_{m2}, \ldots, b_{1n} \ldots b_{mn} \end{bmatrix}^T \in \Re^{m \cdot n}. \tag{28}$$

B. CTSMC Using MLNN

The MLNN is designed to approximate the uncertain nonlinear function in this article. In order to achieve this goal, the current tracking error is used as the input signal of the NN.

Assumption 2: There are optimal parameters that can make the approximation effect of the NN the best for which the following equation can be obtained:

$$f(x) = W^{*T} h^*(x, c^*, b^*, W_{r1}^*, W_{r2}^*) + \varepsilon \tag{29}$$

where W^*, c^*, b^*, W_{r1}^*, and W_{r2}^* are the optimal parameters. ε is an approximation error as a bounded parameter.

Therefore, the approximation error of the NN is given as follows:

$$\begin{aligned} f(x) - \hat{f}(x) &= W^{*T} h^* - \hat{W}^T \hat{h} + \varepsilon \\ &= W^{*T} (\hat{h} + \tilde{h}) - \hat{W}^T \hat{h} + \varepsilon \\ &= W^{*T} \hat{h} + W^{*T} \tilde{h} - \hat{W}^T \hat{h} + \varepsilon \\ &= \tilde{W}^T \hat{h} + \hat{W}^T \tilde{h} + \tilde{W}^T \tilde{h} + \varepsilon \end{aligned} \tag{30}$$

where $\tilde{W} = W^* - \hat{W}$ and $\tilde{h} = h^* - \hat{h}$, $\hat{W}$ and $\hat{h}$ are the actual weight and output signal of hidden layer nodes, respectively. $\tilde{W}^T \tilde{h} + \varepsilon = \varepsilon_0$ is the lumped approximation error. In order to obtain the parameter learning laws of the MLNN, the Taylor expansion of $\tilde{h}$ is performed so that the expansion can be derived as follows:

$$\tilde{h} = \left.\frac{\partial \tilde{h}}{\partial c}\right|_{c=\hat{c}} (c^* - \hat{c}) + \left.\frac{\partial \tilde{h}}{\partial b}\right|_{b=\hat{b}} \left(b^* - \hat{b}\right) + \left.\frac{\partial \tilde{h}}{\partial W_{r1}}\right|_{W_{r1}=\hat{W}_{r1}} \left(W_{r1}^* - \hat{W}_{r1}\right)$$

$$+\left.\frac{\partial \tilde{h}}{\partial W_{r2}}\right|_{W_{r2}=\hat{W}_{r2}}\left(W_{r2}^{*}-\hat{W}_{r2}\right)+\Delta$$
$$=Dh(c)\cdot\tilde{c}+Dh(b)\cdot\tilde{b}+Dh(W_{r1})\cdot\tilde{W}_{r1}+Dh(W_{r2})\cdot\tilde{W}_{r2}+\Delta \tag{31}$$

where Δ is a high-order term. By substituting (31) into (32), the high-order lumped approximation error term $\tilde{W}^T\Delta+\varepsilon_0$ can be obtained and it is assumed to be bounded by $|W^T\Delta+\varepsilon_0|\le\Delta_d$, where Δ_d is a positive constant. Meanwhile, $\tilde{c}$, $\tilde{b}$, $\tilde{W}_{r1}$, and $\tilde{W}_{r2}$ are written as follows:

$$\tilde{c}=[\tilde{c}_{11}\ldots\tilde{c}_{m1}\ldots\tilde{c}_{1n}\ldots\tilde{c}_{mn}]^T,\quad \tilde{W}_{r1}=[\tilde{W}_{r11}\tilde{W}_{r12}\ldots\tilde{W}_{r1m}]^T$$
$$\tilde{b}=[\tilde{b}_{11}\ldots\tilde{b}_{m1}\ldots\tilde{c}_{1n}\ldots\tilde{c}_{mn}]^T,\quad \tilde{W}_{r2}=[\tilde{W}_{r21}\tilde{W}_{r22}\ldots\tilde{W}_{r2m}]^T.$$

And $Dh(c)$, $Dh(b)$, $Dh(W_{r1})$, and $Dh(W_{r2})$ are expressed as follows:

$$Dh(c)=\begin{bmatrix}\frac{\partial h_1}{\partial c_{11}} & \cdots & \frac{\partial h_1}{\partial c_{mn}}\\ \vdots & \ddots & \vdots\\ \frac{\partial h_n}{c_{11}} & \cdots & \frac{\partial h_n}{\partial c_{mn}}\end{bmatrix}_{n\times mn} \tag{32}$$

$$Dh(b)=\begin{bmatrix}\frac{\partial h_1}{\partial b_{11}} & \cdots & \frac{\partial h_1}{\partial b_{mn}}\\ \vdots & \ddots & \vdots\\ \frac{\partial h_n}{\partial b_{11}} & \cdots & \frac{\partial h_n}{\partial b_{mn}}\end{bmatrix}_{n\times mn} \tag{33}$$

$$Dh(W_{r1})=\begin{bmatrix}\frac{\partial h_1}{\partial W_{r11}} & \cdots & \frac{\partial h_1}{\partial W_{r1m}}\\ \vdots & \ddots & \vdots\\ \frac{\partial h_n}{\partial W_{r11}} & \cdots & \frac{\partial h_n}{\partial W_{r1m}}\end{bmatrix}_{n\times m} \tag{34}$$

$$Dh(W_{r2})=\begin{bmatrix}\frac{\partial h_1}{\partial W_{r21}} & \cdots & \frac{\partial h_1}{\partial W_{r2n}}\\ \vdots & \ddots & \vdots\\ \frac{\partial h_n}{\partial W_{r21}} & \cdots & \frac{\partial h_n}{\partial W_{r2n}}\end{bmatrix}_{n\times n}. \tag{35}$$

Theorem 2: Based on the above-mentioned complementary terminal sliding surface (10) and (11), NN and dynamic model (3), the intelligent CTSMC using MLNN estimator can be designed as (36)–(38), and the learning laws for MLNN parameters are chosen as (39)–(43) to ensure the closed-loop stability of the control system

$$u_{\text{eq}}=-\frac{1}{b}\left[\hat{f}(x)-\ddot{x}_r+\lambda(2\dot{e}+me^{m-1}\dot{e}+\lambda e^m+\lambda e)+\lambda s_c\right] \tag{36}$$

$$u_{\text{sw}}=-\frac{1}{b}K_w\text{sgn}(s+s_c) \tag{37}$$

$$u=u_{\text{eq}}+u_{\text{sw}} \tag{38}$$

$$\dot{\hat{W}}=-\eta_1(S_g+S_c)\hat{h} \tag{39}$$

$$\dot{\hat{b}}^T=-\eta_2(S_g+S_c)\hat{W}^TDh(b) \tag{40}$$

$$\dot{\hat{c}}^T=-\eta_3(S_g+S_c)\hat{W}^TDh(c) \tag{41}$$

$$\dot{\hat{W}}_{r1}^T=-\eta_4(S_g+S_c)\hat{W}^TDh(W_{r1}) \tag{42}$$

$$\dot{\hat{W}}_{r2}^T=-\eta_5(S_g+S_c)\hat{W}^TDh(W_{r2}) \tag{43}$$

where η_1, η_2, η_3, η_4, and η_5 are learning rate parameters and all are set as positive constants.

Proof: Considering a Lyapunov function candidate as follows:

$$V_2=\frac{1}{2}s^Ts+\frac{1}{2}\text{tr}\left(\tilde{W}^T\eta_1\tilde{W}\right)+\frac{1}{2}\text{tr}\left(\tilde{b}^T\eta_2\tilde{b}\right)$$
$$+\frac{1}{2}\text{tr}\left(\tilde{c}^T\eta_3\tilde{c}\right)+\frac{1}{2}\text{tr}(\tilde{W}_{r1}^T\eta_4\tilde{W}_{r1})+\frac{1}{2}\text{tr}\left(\tilde{W}_{r2}^T\eta_5\tilde{W}_{r2}\right). \tag{44}$$

Taking the time derivative of the Lyapunov function and using (36)–(42), one can derive

$$\begin{aligned}\dot{V}_2=&-\lambda(S_g+S_c)^2+(S_g+S_c)\Big[\Delta_d-K_w\text{sgn}(S_g+S_c)\\&+d(t)\Big]\\ \le&-\lambda(S_g+S_c)^2+|S_g+S_c|\left(\Delta_d+d(t)\right)\\&-K_w(S_g+S_c)\\ \le&-\lambda(S_g+S_c)^2-|S_g+S_c|\left(K_w-\Delta_d-d(t)\right).\end{aligned} \tag{45}$$

Setting the sliding-mode gain $K_w\ge(\Delta_d+|d(t)|)$. $\dot{V}_2\le 0$ can be obtained. Then, the negative semidefinite of $\dot{V}_2$ guarantees that all signals contained in (44) are bounded. Furthermore, according to Barbalat's lemma, sliding mode S_g and S_c and tracking error e will converge to zero as $t\to\infty$.

Base on the above analysis, the design procedure of the proposed CTSMC-MLNN scheme can be summarized step-by-step as follows.

Step 1: First, the tracking error and sliding-mode surfaces are deduced by (6), (10), and (11).

Step 2: Relevant parameters of the CTSMC are determined, especially the gain K_w, which plays an important role in the chattering phenomenon.

Step 3: The initial values of the parameters of MLNN are determined. The initial values of output weight and weight of the internal feedback loop are chosen as $W=W_{r2}=$ones (1, node). The node is the number of neurons in the hidden layer. The initial value of the weight of external feedback loop is chosen as $W_{r1}=1$. It is worth noting that the initial value of C and B should be chosen according to the approximate range of the input signal and are chosen by experts as $C=[\ 1\quad 0.5\quad -0.5\quad -1\ ]$ and $B=0.602\,^*$ones (1, node). The specific reasons will be discussed in the following text.

Step 4: The learning laws are derived as (39)–(43), and then the intelligent CTSMC laws are obtained by (36)–(38). Finally, the learning law of all parameters is adjusted until the requirements are met.

Remark 2: In this article, because the object approximated by the NN is strongly nonlinear, the five parameters of MLNN are obtained through online learning, which will inevitably lead to an increase in the computational burden. Furthermore, the

TABLE I
COMPUTATIONAL TIME COMPARISON

Methods	SMC	CTSMC	RBFNN	MLNN	DHLRNN[29]
Time(s)	9.303	10.042	25.194	49.737	75.641

mean value and standard deviation of the hidden layer are very special, and their selection is dependent on the distribution of the input signal. The closer the mean value C is to the input signal, the higher the sensitivity of the Gaussian function. Generally speaking, standard deviation B should be chosen larger to obtain a wider Gaussian function and a stronger ability of mapping the input. Therefore, the selection of B is determined by the amplitude range of the input signal and designed to be a moderate value. Thus, the five parameters of the MLNN are obtained through online learning because all parameters are related to the input signal of the hidden layer. Meanwhile, the computational burden of MLNN will be analyzed and compared below.

Remark 3: The mean value of the Gaussian function of the traditional RBFNN can be determined when the distribution of the input sample data is representative. Thus, the nonlinear mapping relationship of RBFNN is also determined [30]. Because the relationship of the output of the RBFNN and output weight is linear, the output weight can be obtained by solving the linear equations. This greatly accelerates the learning speed and avoids the problem of local minima [31]. However, the parameters of MLNN are updated online through the adaptive law (39)–(43) in this article. The selection of their learning rate is difficult to be optimal, which will inevitably lead to the problem of local optima. Therefore, the optimization of the parameters update method will be future work.

Remark 4: The updating of the parameters of NN requires matrix operation and partial derivative calculation, which is the reason that the computational burden of the method using NN is bound to increase compared with the traditional SMC. Table I presents the calculation time of five methods in simulation study. In order to exclude the influence of other factors, the computational time of all NN control algorithms in the table only counts the operation time of NN modules and the number of neurons in NN is the same. Although the computational complexity is increased, the computational burden of MLNN is relatively small on the premise of meeting the performance requirement of APF. However, further optimization is needed.

V. SIMULATION STUDY

In order to verify the proposed control scheme, several simulation studies are carried out in this section. The effectiveness of the proposed controller is verified by MATLAB/Simulink package.

A. Simulation Parameter Configuration

In the simulation, relevant parameters of the APF simulation model are shown in Table II.

In this article, the SAPF control system is divided into two parts, one is the dc-side voltage control and the other is the current control. Due to the low accuracy requirements of the voltage control, this article selects the traditional PI control to control the dc-side voltage. However, the current control accuracy requirement is very high. Therefore, it is very important to choose the parameters of NN and sliding surface. The parameters of the PI controller and the proposed control algorithm are chosen as $K_p = 0.15$ and $K_I = 0$. In order to simulate the influence of the uncertainty of APF parameters in the practical application, the parameters of the APF main circuit in Table II are used in the algorithm design, but in the Simulink model, the parameters of the APF are set as $R_{\text{ac}} = 1\,\Omega$ and $L_{\text{ac}} = 18\,\text{mH}$.

TABLE II
APF MODEL PARAMETERS

Parameters	Values
Supply voltage	$U_s = 24\,V$, $f = 50\,Hz$
Steady load	$R_1 = 5\,\Omega$, $R_2 = 15\,\Omega$, $C = 1e^{-3}\,F$
Dynamic load	$R_1 = 15\,\Omega$, $R_2 = 15\,\Omega$, $C = 1e^{-3}\,F$
APF main circuit parameters	$R = 0.1\,\Omega$, $L = 10\,mH$, $C = 2.2e^{-3}\,F$, $U_{dc}^{*} = 50\,V$
Sample time	$T_s = 1e^{-5}s$

TABLE III
PARAMETERS OF FOUR ALGORITHMS

SMC	$K_w = 3e^9$, $\lambda = 4e^3$
CTSMC	$K_w = 3e^9$, $\lambda = 4e^3$, $p = 5$, $q = 3$
FNN	$\eta_m = 0.1$, $\eta_\sigma = 0.6$, $\eta_w = 0.4$
CTSMC-MLNN	$K_w = 5e^5$, $\lambda = 1e^3$, $p = 5$, $q = 3$ $\eta_1 = 8.8e^6$, $\eta_2 = 1$, $\eta_3 = 1$, $\eta_4 = 0.005$, $\eta_5 = 0.02$

In order to prove the superiority of complementary terminal sliding mode and the approximation effect of MLNN, three algorithms, SMC, CTSMC, and CTSMC-MLNN, are applied to the APF model. In addition, a widely used fuzzy neural network (FNN) structure [32], [33], [34] is also introduced as a comparison method, and its parameter learning is also referred to the above relevant pieces of literature. The parameters of the four algorithms are shown in Table III, where η_m, η_σ, and η_w are the learning rate of means, standard deviations in membership layer of FNN, and output weight in the output layer, respectively.

B. Steady-State Simulation Results and Analysis

In the simulation, the APF is connected to the grid at 0.05 s. Fig. 4 contains the images of load current, compensation current, and grid current after compensation (from top to bottom). Because of the existence of a nonlinear load, the load will send back part of the nonsinusoidal wave to the power grid when the power supply supplies power to the load, resulting in serious current distortion. After connecting the APF to the grid, the compensation current enters the grid, the harmonic current is compensated, and the grid current quickly becomes a sine wave.

In addition, Fig. 5 shows the diagram of compensation current (blue curve) tracking reference current (red curve) in the first

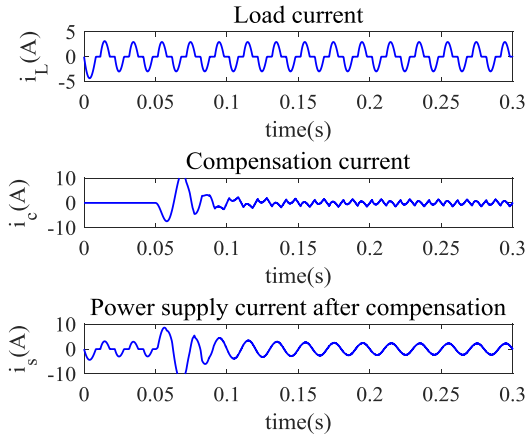

Fig. 4. Current curve of the steady-state response.

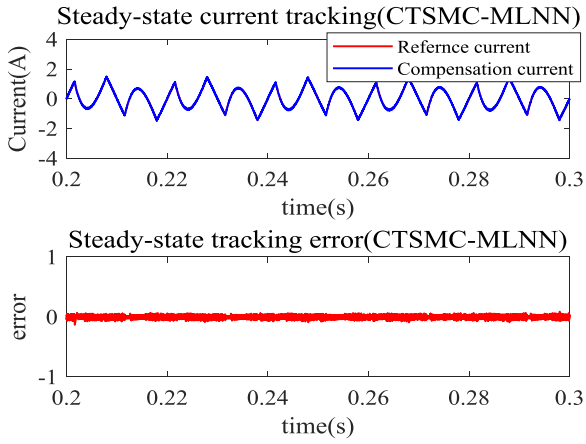

Fig. 5. Current tracking comparison curve and error curve under steady-state response.

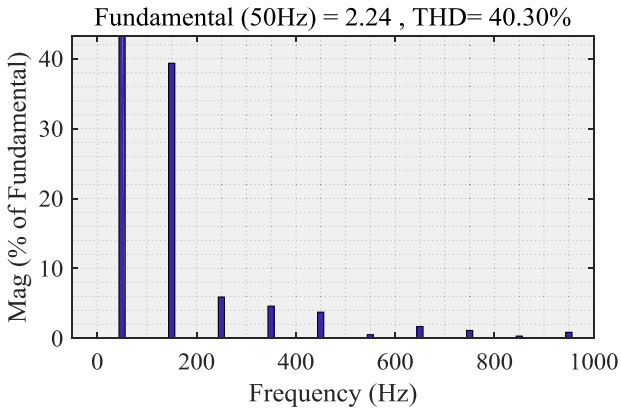

Fig. 6. Grid current spectrum analysis before compensation.

figure and tracking error waveform under steady-state conditions. The reference current is calculated by the harmonic detection algorithm and the compensation current is obtained by controlling IGBT switches.

Figs. 6 and 7 show the spectrum analysis of the power grid current before and after compensation. Before APF is connected,

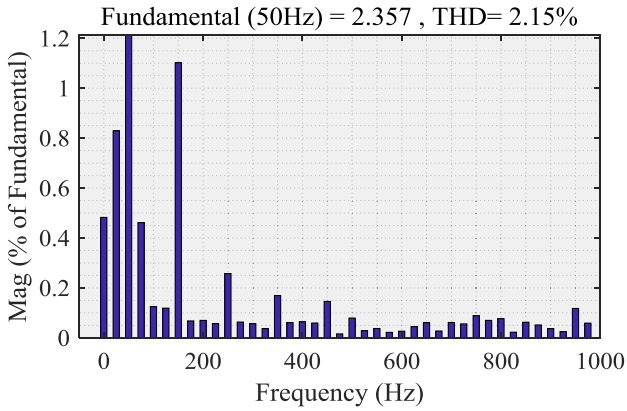

Fig. 7. Grid current spectrum analysis after compensation.

the total harmonic disturbance (THD) of the grid current was 40.30%, which is far higher than the international standard of 5%. After the APF is connected, the THD of the grid current drops to 2.15%, which indicates that the APF using the proposed control method has good harmonic suppression capability.

In addition to suppressing harmonics, APF can also compensate the reactive power on the load side. This article proves this capability of APF by calculating the power factor (PF). The formula for calculating PF is given as follows:

$$\begin{aligned} \mathrm{PF} &= \frac{I_{S_1}}{I_S}\cos\phi_0 = \frac{I_{S_1}}{\sqrt{I_{S1}^2 + \sum_{n=2}^{\infty} I_{Sn}^2}}\cos\phi_0 \\ &= \frac{1}{\sqrt{1+\mathrm{THD}^2}}\cos\phi_0 \end{aligned} \tag{46}$$

where I_{S_1} and I_S are the effective value of the fundamental wave current and the total current, respectively. ϕ_0 is a fundamental wave displacement angle, that is, the phase angle between the voltage and fundamental wave current. It is not difficult to know that the key of calculating PF is to calculate ϕ_0.

In order to easily observe the change of the fundamental wave displacement angle ϕ_0 before and after compensation, the amplitude of the voltage waveform is reduced. Fig. 8 shows the waveforms of power supply voltage and current before and after compensation. When APF is not connected to the grid, the fundamental wave displacement angle ϕ_0 is $9.9007°$; therefore, PF is 0.9296. When harmonic current is compensated, the ϕ_0 is $0.2693°$ and the PF is 0.9998. Obviously, APF based on the proposed control strategy can excellently compensate reactive power of the load and improve the efficiency of electrical equipment.

C. Dynamic Simulation Results and Analysis

A nonlinear load is connected in parallel at 0.3 s and the nonlinear load is removed at 0.6 s to simulate the actual power supply process. In order to show the effect of CTSMC and MLNN, respectively, three strategies are designed to verify the superiority of the proposed method.

Fig. 9 plots the dynamic response of grid current after compensation using the CTSMC-MLNN method showing whether

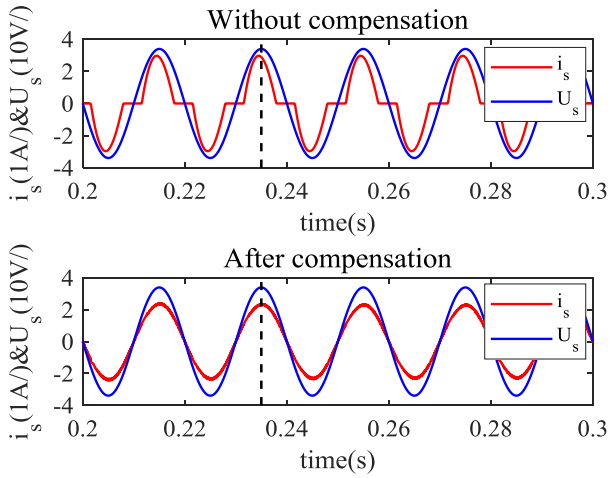

Fig. 8. Power supply voltage and current waveforms before and after compensation.

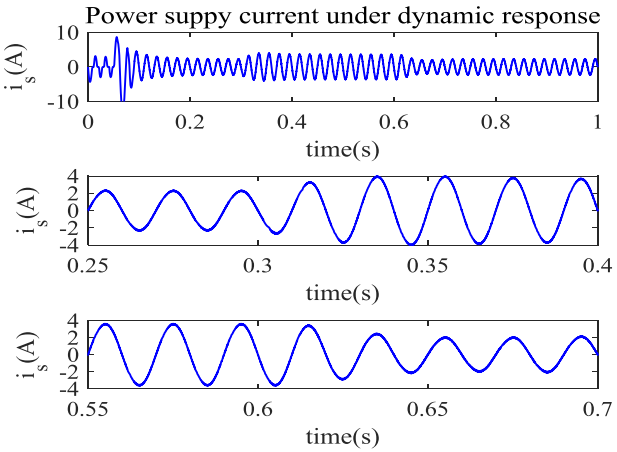

Fig. 9. Grid current after compensation under CTSMC-MLNN.

a nonlinear load is connected in parallel at 0.3 s, or the load is removed at 0.6 s, the grid current can change smoothly and quickly become a standard sine wave, demonstrating that the proposed method has a fast dynamic response.

Furthermore, the current tracking comparison curve and error curve are given in Fig. 10 and Fig. 11, respectively. It is obvious that the compensation current can always accurately track the reference current whether the load suddenly increases at 0.3 s or suddenly decreases at 0.6 s. At the same time, it is observed the error curve can achieve a smooth transition around these two moments from Fig.11, which also illustrates that even if there is a parameter uncertainty and the external load changes, the APF system with the proposed algorithm still has good harmonic tracking accuracy.

Figs. 12 and 13 show the spectrogram of the power supply current after the load is increased and decreased, respectively. After a load is connected in parallel, the THD of the grid current is measured as 1.56% at 0.4 s, and after the load is removed, the THD is 2.32% at 0.7 s. This fully demonstrates that the

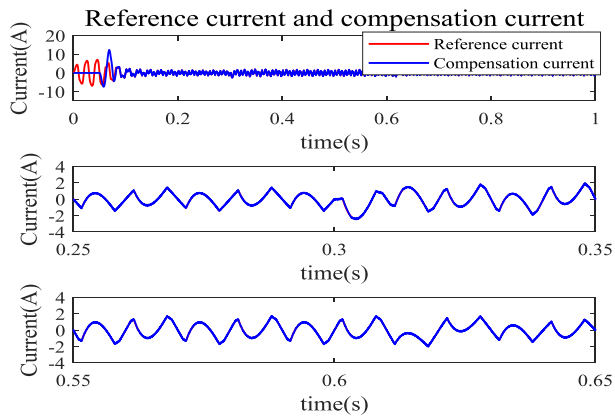

Fig. 10. Current tracking comparison and its local enlarged curve under dynamic response.

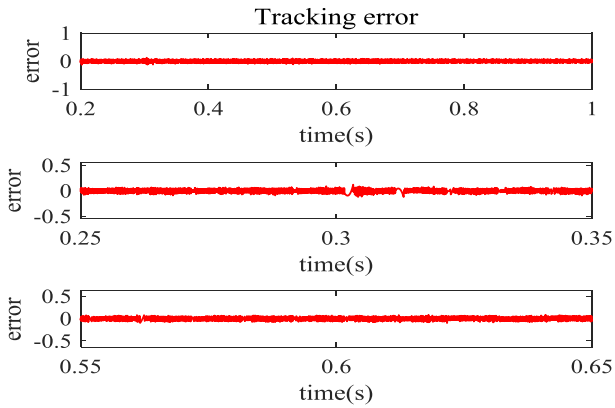

Fig. 11. Current tracking error and its local enlarged curve under dynamic response.

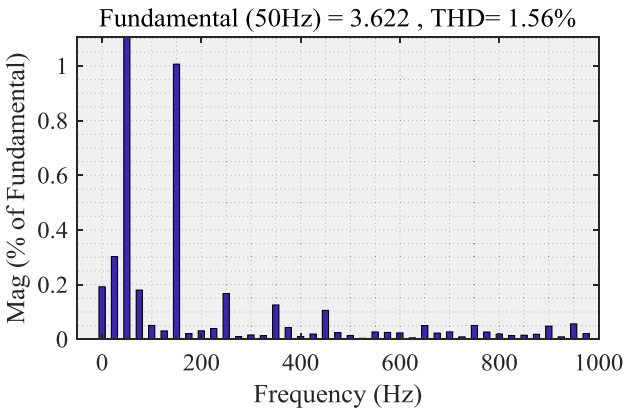

Fig. 12. Spectrogram of power supply current after the load is increased (0.4 s).

load change has little influence on the realization of the control objective.

Moreover, the reference signal changes at the moment of 0.3 s and 0.6 s' load sudden changes, which will lead to the emergence of an inevitable dynamic error. At this time, the harmonics will also increase instantaneously. Figs. 14 and 15 are spectrograms of power supply current at 0.3 s and 0.6 s, respectively. It is

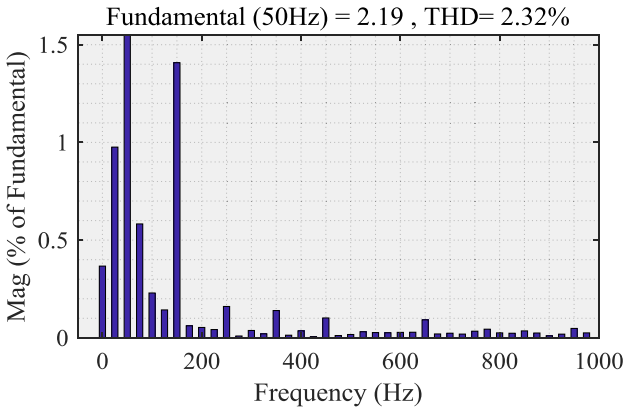

Fig. 13. Spectrogram of power supply current after the load is decreased (0.7 s).

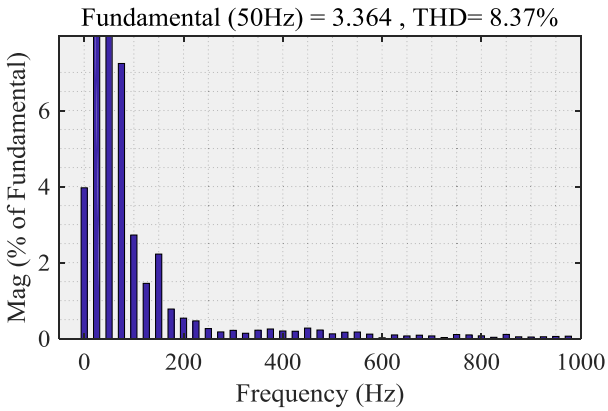

Fig. 14. Spectrogram of power supply current when the load is increased suddenly (0.3 s).

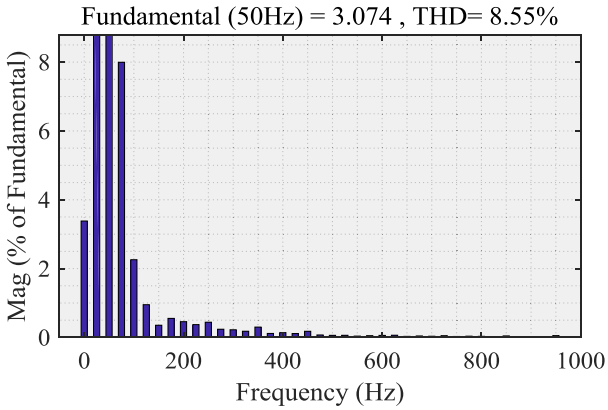

Fig. 15. Spectrogram of power supply current when the load is decreased suddenly (0.6 s).

observed that a sudden increase in the low-order harmonics compared with the steady state and the THD is 8.37% when load increases. The situation is also roughly similar when the load of 0.6 s is removed, where the THD is 8.55%. However, the sudden increase of this harmonic is in line with objective laws and is acceptable. Because after 0.04 s, the THD value of the

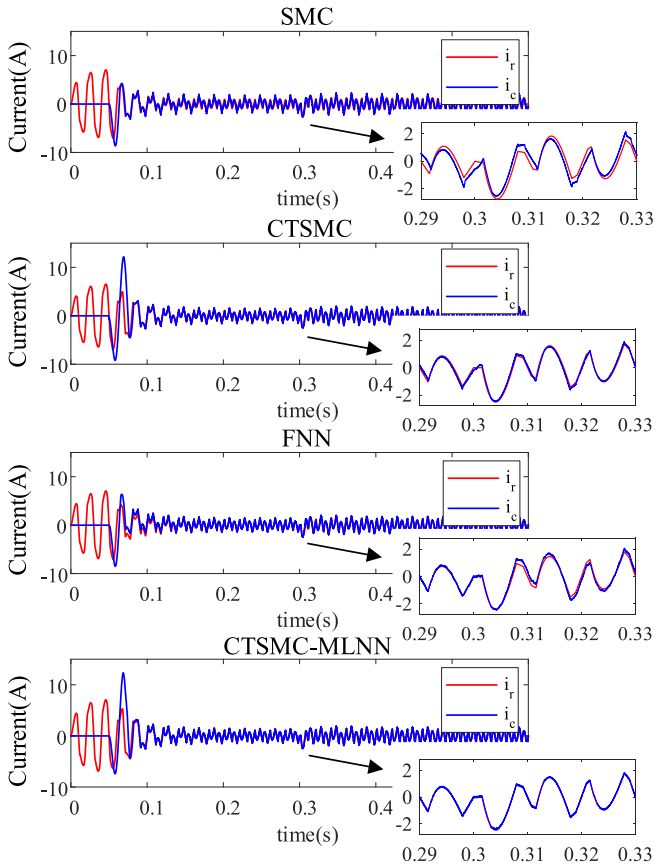

Fig. 16. Current tracking compensation curve under three methods.

power supply current returns to a low level, which are 1.71% at 0.34 s and 3.25% at 0.64 s.

D. Simulation Comparison Analysis

Simulation comparison with the traditional SMC, CTSMC strategy, and FNN controller is discussed in the following procedure.

Fig. 16 shows the curve of compensation current for tracking harmonic current under four different methods, and Fig. 17 shows the current tracking error curve under the corresponding method. Obviously, the four methods all can achieve the control target. However, in terms of tracking accuracy, CTSMC is obviously superior to SMC when the two sliding-mode controller parameters are identical. In the meanwhile, a conclusion can also be drawn from Fig. 17, whether it is SMC or CTSMC, their tracking error curves are significantly periodic, which shows that only increasing the sliding-mode gain cannot perfectly suppress the periodic disturbance caused by the unmodeled part. On the contrary, after the nonlinear function $f(x)$ in the model is approximated by the MLNN, the variation range of the tracking error is reduced and the error curve is smoother. In addition, the current tracking error under FNN controller control suddenly increases and maintains 0.03 s when the load changes in 0.3 s and 0.6 s, which shows that the robustness of the FNN control method is inferior to the other three methods, although it does not

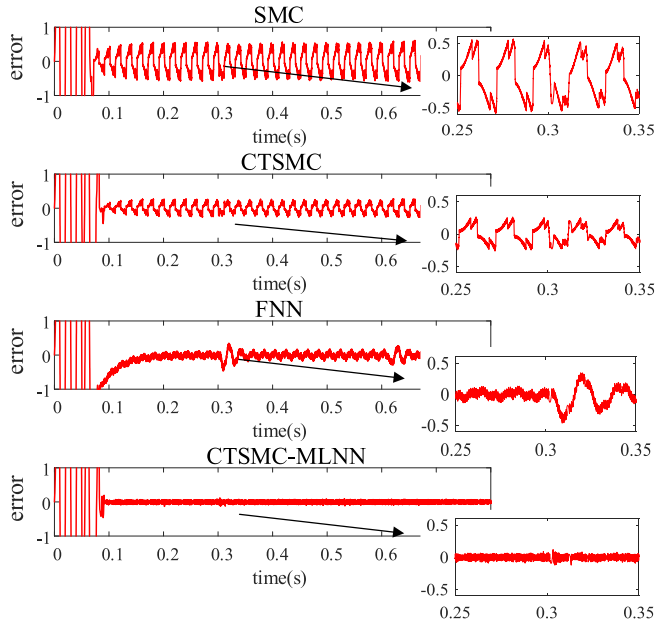

Fig. 17. Tracking error comparison.

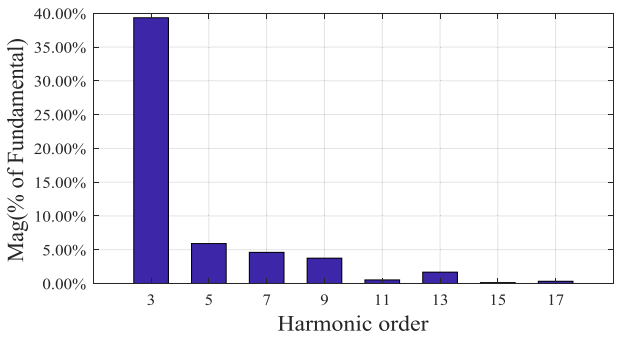

Fig. 18. Load current harmonic spectrum.

need to consider chattering. Considering the SAPF application scenario mentioned above, the continuous change of load will inevitably occur in daily use, which shows that there is a high requirement for the robustness of the current control method. Meanwhile, compared with the SMC theory, although the convergence time of the FNN controller is affected by the learning rate parameters, its exact convergence time or time range cannot be calculated. Therefore, these two figures strongly prove that the proposed method retains the advantages of SMC technology, and the improvement of MLNN on controller performance is also apparent.

Fig. 18 shows the spectrum analysis diagram of load current with harmonic order and magnitude (% of fundamental). It is observed that the magnitude of third, fifth, seventh, and ninth harmonics is, respectively, 39.34%, 5.91%, 4.61%, and 3.75% to that of the fundamental component, which is a high level. These harmonic components wil1 greatly pollute the power grid and reduce the life and safety of electrical equipment. To further verify the validity and superiority of the proposed method in harmonic suppression, the spectrograms of supply current with

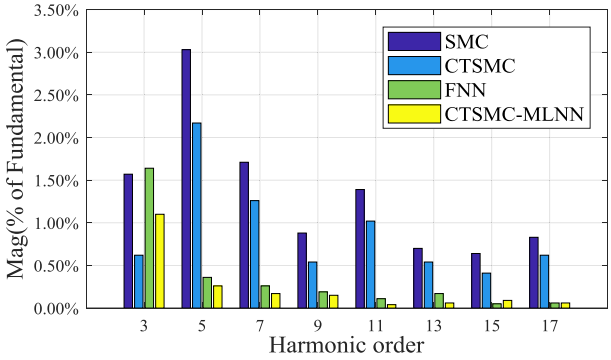

Fig. 19. Power supply current harmonic spectrum comparison under steady state (0.2 s).

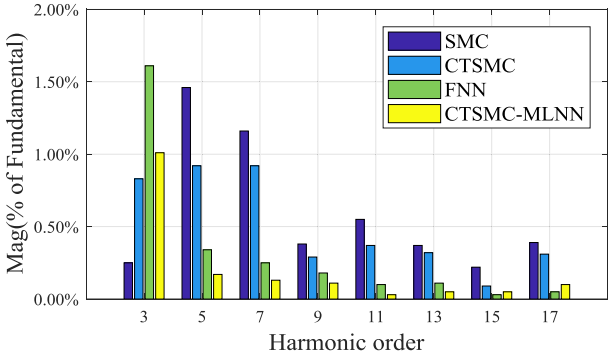

Fig. 20. Power supply current harmonic spectrum comparison after load increase (0.4 s).

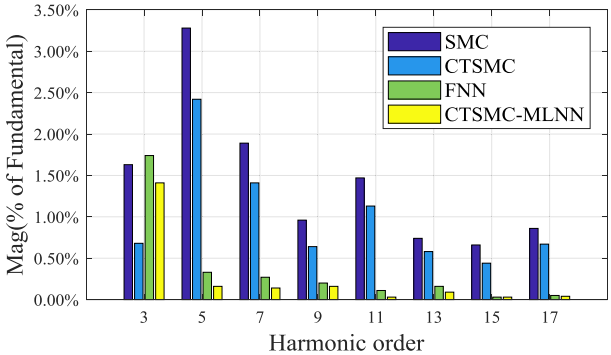

Fig. 21. Power supply current harmonic spectrum comparison after load decrease (0.7 s).

harmonic order and magnitude (% of fundamental) using different control methods under steady-state and dynamic response are shown in Figs. 19–21. It can be clearly seen that, with the proposed algorithm, the magnitude from the 5th harmonic to the 17th harmonic in the power supply current is all lower than 0.5%, which is a very low level. Meanwhile, the change of external load has little effect on the harmonic suppression. Whether the load increases or the load decreases, the harmonics of each order are reduced to a very low level, which also proves that the proposed algorithm retains the advantage of strong robustness

TABLE IV
SYSTEM PERFORMANCE COMPARISON OF DIFFERENT METHODS

State \ Strategy	SMC	CTSMC	FNN	CTSMC-MLNN
Steady-state (0.2s)	4.17%	3.30%	2.73%	2.15%
When load increase (0.3s)	8.70%	8.50%	9.33%	8.37%
After load increase (0.4s)	2.05%	1.88%	2.16%	1.56%
When load decrease (0.6s)	9.12%	8.68%	9.74%	8.55%
After load decrease (0.7s)	4.42%	3.69%	2.98%	2.32%

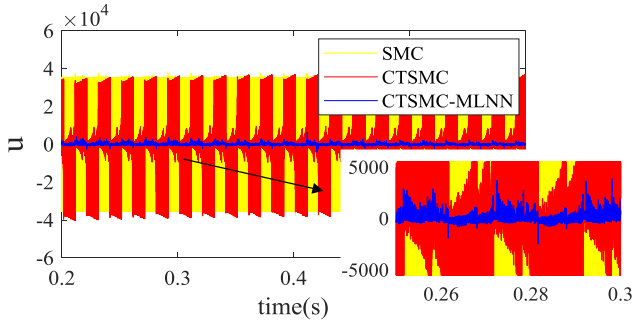

Fig. 22. Control output comparison curve under the three methods.

Table IV presents the THD data of four methods under different conditions. The THD of the CTSMC method under steady state, load increases, and load decreases is 3.30%, 1.88%, and 3.69%, which are 0.87%, 0.17%, and 0.73% lower than SMC under the same condition. Moreover, the THD of the CTSMC-MLNN method is 2.15% under steady-state condition, which is 1.15% lower than that of the CTSMC. The THD of the CTSMC-MLNN method is 1.56% and 2.32%, respectively, after load surges and decreases, which are 0.32% and 1.37% lower than the CTSMC method. The harmonic compensation effect of the FNN controller is also good at steady state and 0.1 s after load change, while the THD value increases significantly at the moment of load change. On the contrary, in the face of load surge and load decrease, the THD index of the proposed algorithm is the lowest among the four methods, which indicates that with the proposed algorithm, the change of the load in the grid has the least influence on the harmonics compensation.

Therefore, according to the steady-state, dynamic response, and comparative analysis, the proposed method maintains the optimal harmonic compensation effect in five cases.

Finally, the chattering comparison of the control output is discussed as follows. Fig. 22 shows the control output comparison curve, which proves that the MLNN can significantly weaken the inherent chattering in SMC. Compared with the traditional SMC method (yellow curve), the CTSMC (red curve) has a smaller control output amplitude range at some periods. Furthermore, the control output of the proposed algorithm (blue curve) changes in the range of -5000 to 5000, which shows the CTSMC-MLNN method has a smaller control amplitude range and output change. In addition, the variance index of the control output is given in Table IV. It can be seen intuitively that the difference in the fluctuation of the control output of the three methods can also verify the conclusion mentioned above.

TABLE V
COMPARISON OF OUTPUT CHATTERING

Index \ Strategy	SMC	CTSMC	CTSMC-MLNN
Output variance	0.2204	0.0297	0.0052

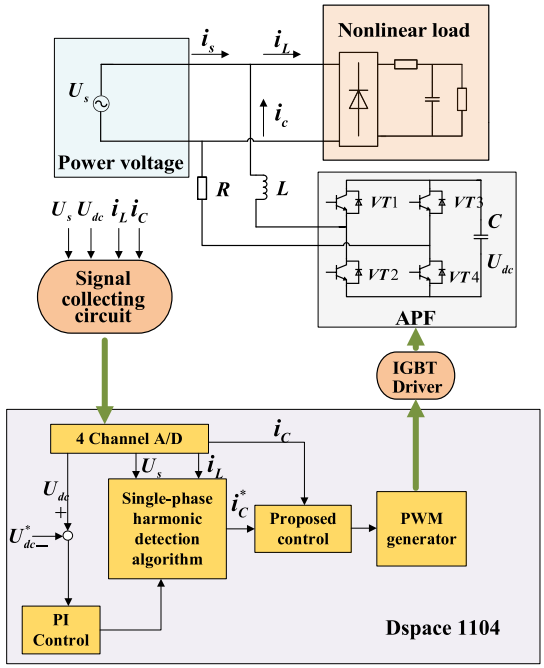

Fig. 23. Structure diagram of SAPF prototype.

Remark 5: Output chattering is an important index of a system, especially the power electronic system with high-frequency switches, such as APF. In order to explore the chattering severity of the three methods, the control output signal $u(t)$ at a steady state (0.2–0.3 s) was collected and standardized as follows:

$$u(t)^* = \frac{u(t) - u(t)_{\max}}{u(t)_{\max} - u(t)_{\min}}. \tag{47}$$

Then, the variance of the normalized control signal $u(t)^*$ is calculated, as shown in Table V.

VI. EXPERIMENTAL STUDY

A. Overall Structure of APF Prototype

In this section, hardware experiments are used to further verify the feasibility of the proposed algorithm. The structure diagram of the hardware platform of SAPF is presented in Fig. 23. It mainly includes six parts: power voltage module, APF main circuit module, IGBT drive module, signal detection module, nonlinear load module, and dSPACE 1104 control module. The specific workflow is given as follows: First, the signal collecting circuit obtains the corresponding voltage and current signals, which are power supply voltage: U_s, dc-side voltage $U_{\rm dc}$, load current i_L, and compensation current i_c through sensors, and

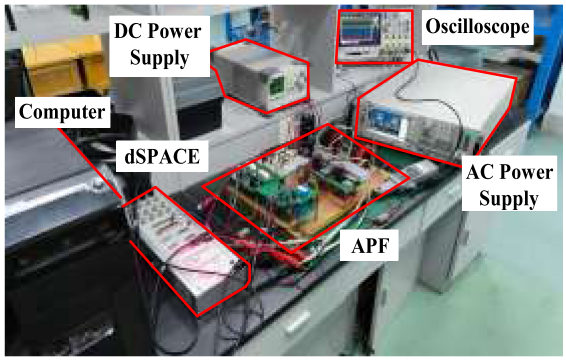

Fig. 24. Overall structure of APF prototype.

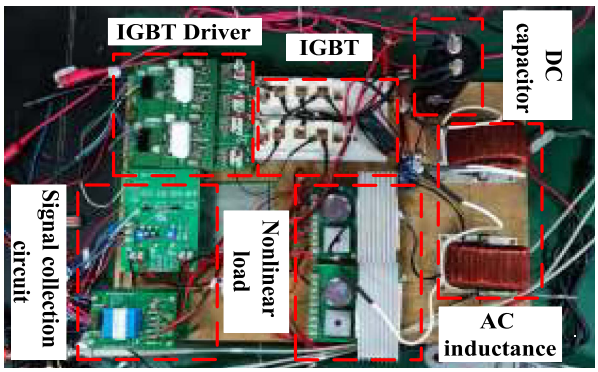

Fig. 25. Main circuit diagram of APF prototype.

then transmits them to dSPACE 1104 control module through the four-channel A/D. Second, the reference signal is calculated by a single-phase harmonic detection algorithm. Then, the dc-side voltage adopts the PI controller to stabilize the capacitor voltage and the current loop control signal is calculated by the proposed algorithm. Finally, the control signal is pulsewidth modulation modulated and sent to the IGBT drive circuit, and then the IGBT drive circuit controls the turn-ON and turn-OFF of the IGBT in the circuit to adjust and control compensation current.

The physical diagram of the single-phase low-voltage APF experimental prototype is shown in Fig. 24. The hardware experimental equipment mainly includes APF main circuit, personal computer, dc source, ac source, and dSPACE 1104. Fig. 25 shows the main circuit diagram of the single-phase low-voltage APF prototype. The control system parameters of the experimental prototype are presented in Table VI.

TABLE VI
SYSTEM PARAMETERS FOR EXPERIMENT

Parameter	Value
Supply voltage and frequency	$U_s = 24\,V$, $f = 50\,Hz$
Nonlinear load	$R_1 = 5\,\Omega$, $R_2 = 15\,\Omega$, $C = 1e^{-3}\,F$
Additional nonlinear loads in parallel	$R_1 = 15\,\Omega$, $R_2 = 15\,\Omega$, $C = 1e^{-3}\,F$
Main circuit	$R_c = 0.1\,\Omega$, $L_c = 10\,mH$, $C = 2.2e^{-3}\,F$, $U_{dc}^{*} = 50\,V$
Sampling time	$T_s = 5e^{-5}s$
AC source	IT7324, ITECH
Power IGBTs	SKM75GB12T4, SEMIKON
Voltage sensors	SKYPER_32_R, SEMKION
Current sensors	CSM003A, CHIEFUL
Auxiliary power supply	DP831, RIGOL

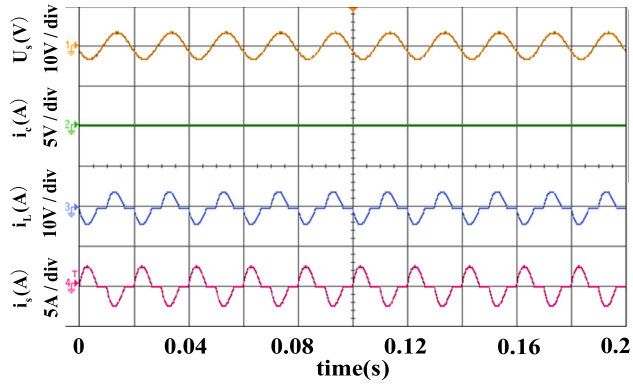

Fig. 26. Waveform diagram of voltage and current before compensation.

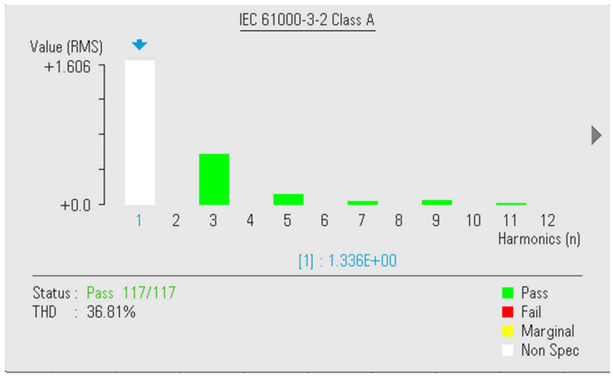

Fig. 27. Harmonic spectrum of source current when APF is not connected.

B. Steady-State Experimental Results and Analysis

Fig. 26 presents the waveform curve before compensating harmonics. The four signal waveforms are, from top to bottom, power supply voltage U_s, compensation current i_c, load current i_L, and power supply current i_s. The first three signals are the converted signals of voltage and current sensors, and the power supply current i_s at the bottom is measured by the current probe. It is worth noting that due to the turn ratio of the sensor, the amplitude of all signals obtained through the sensor is reduced. Therefore, in dSPACE, in order to calculate the accurate harmonic component i_c and control law, these signals need to be restored through the gain module in the real-time simulation model after A/D conversion. At the same time, these restored signals all can be observed in the observation software Control Desk matched with dSPACE. Obviously, the power supply current has serious distortion. Fig. 27 shows the harmonic spectrum of the source current when APF is not

TABLE VII
UPPER LIMIT OF THD IN IEEE 519-2014 STANDARD

Bus voltage in PCC（V/kV）	upper limit of THD (%)
$U_s < 69\ kV$	5
$69\ kV < U_s < 161\ kV$	2.5
$161\ kV < U_s$	1.5

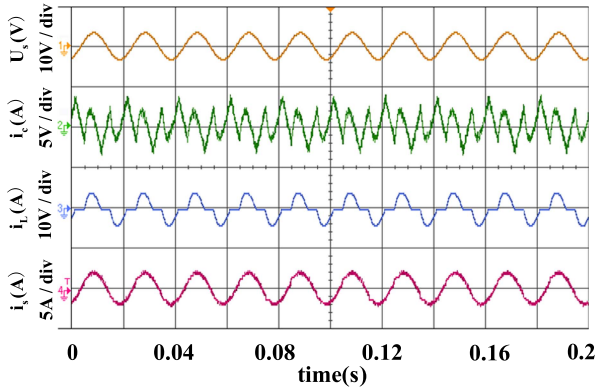

Fig. 28. Steady-state response using CTSMC-MLNN.

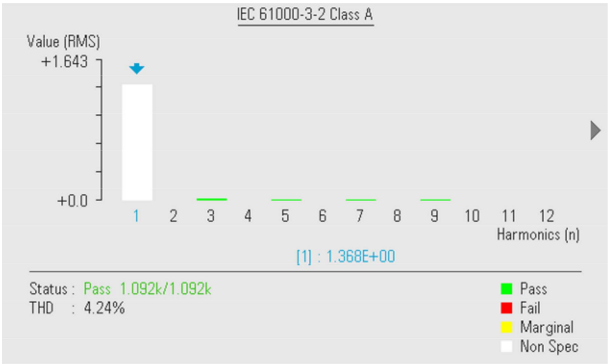

Fig. 29. Power supply current spectrogram using CTSMC-MLNN.

connected. The THD is 36.81%, which is far above international standards, as shown in Table VII. Because the hardware platform built in this article is a low-voltage system, the THD of i_s needs to be less than 5% to meet IEEE 519-2014 standard published by the Institute of Electrical and Electronics Engineers.

Fig. 28 shows the steady-state response curve after connecting APF to the grid. Obviously, the supply current becomes a standard sine wave, and the phase difference between the supply voltage and the supply current is almost zero. This phenomenon shows that the APF not only compensates the harmonics in the power supply current but also compensates the reactive power. Fig. 29 presents the harmonic spectrum of source current under steady-state response where its THD is 4.24%.

C. Dynamic Experimental Results and Analysis

Figs. 30 and 31 show the dynamic response curve of load increases and decreases, respectively, in the hardware experiment. Apparently, a nonlinear load is suddenly connected in parallel

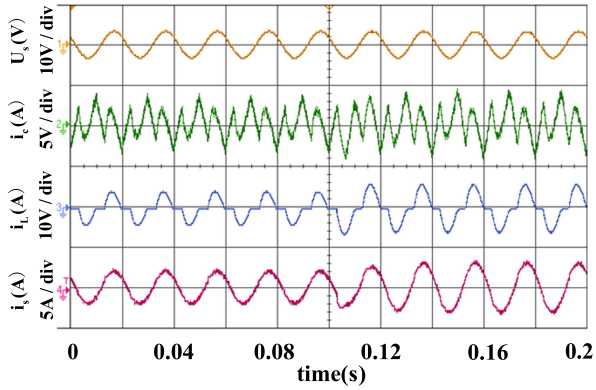

Fig. 30. Dynamic response curve of load increase using CTSMC-MLNN.

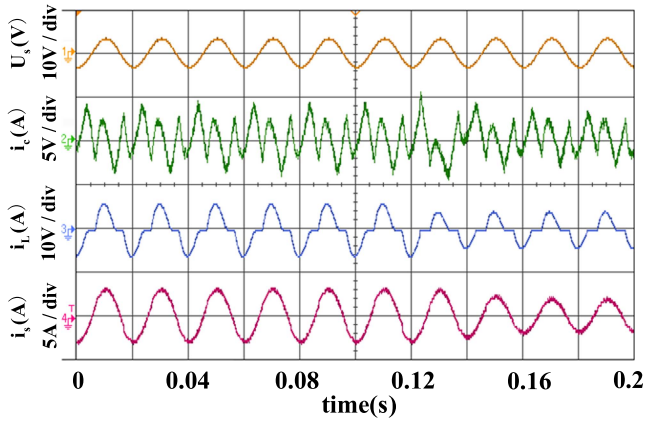

Fig. 31. Dynamic response curve of load decrease using CTSMC-MLNN.

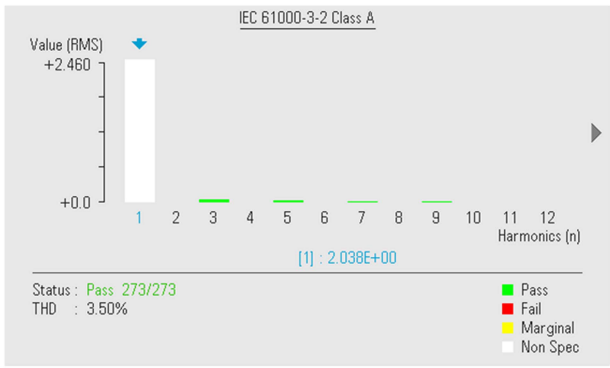

Fig. 32. Power supply current spectrogram after the load increases.

in the circuit, resulting in an increase in the amplitude of the power supply current and load current, as shown in Fig. 30. On the contrary, the amplitude of the power supply current and load current decrease when the load is removed, as shown in Fig. 31.

Fig. 32 shows the spectrogram of the power supply current after the load increases where its THD is 3.50%, and Fig. 33 shows the frequency spectrum of the power supply current after the load is decreased where its THD is 4.70%, which indicates that the APF system using the proposed control method has good dynamic response. The experimental results show

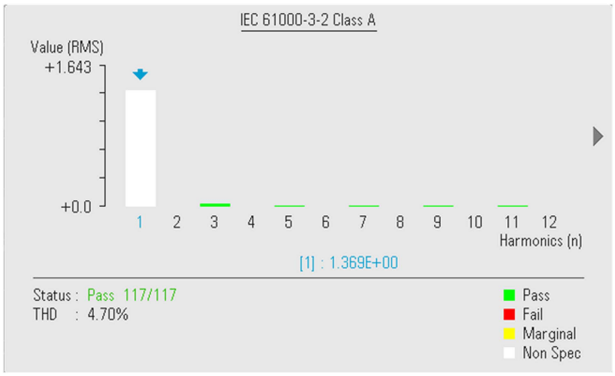

Fig. 33. Dynamic response curve of load decrease using CTSMC-MLNN.

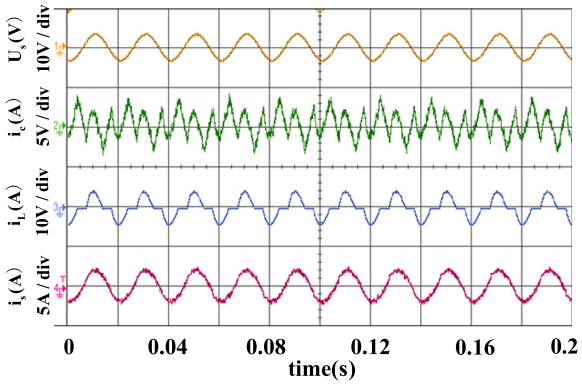

Fig. 34. Steady-state response curve of the comparison method.

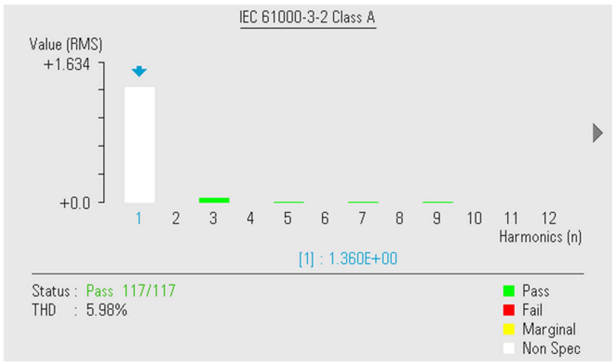

Fig. 35. Power supply current spectrum graph under the steady-state response of the comparison method.

that the compensation performance of APF is good in both steady-state and dynamic conditions, which also proves the feasibility of the proposed control method.

D. Comparison Experiment and Analysis

In order to verify the superiority of the proposed method, the comparison experiments are carried out in this section. Fig. 34 shows the steady-state response curve using the CTSMC method and Fig. 35 presents the corresponding steady-state spectrum, where the THD of the power supply current is 5.98%, which is 1.74% higher than the proposed method. Meanwhile, Figs. 36 and 37 show the voltage and current curve of the CTSMC method after the load increases and the load decreases, respectively. Figs. 38 and 39 show that the corresponding power supply current spectrograms are 5.56% and 6.29%, which are 2.06% and 1.59% higher than the proposed method.

Moreover, the THD comparison results with the traditional SMC, CTSMC, and proposed method are presented in Table VIII, showing that the THD index of the intelligent CTSMC method is smaller than of the other two methods in

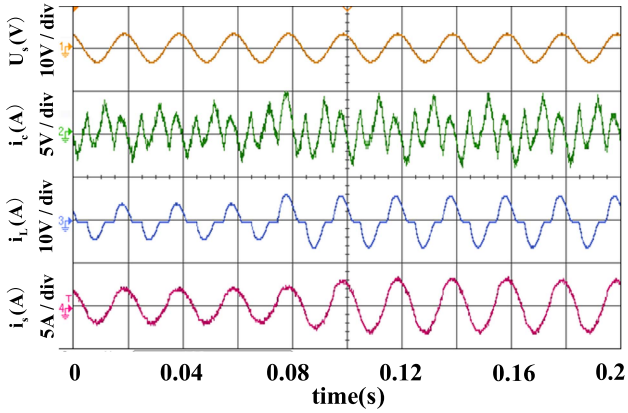

Fig. 36. Dynamic response curve of the comparison method.

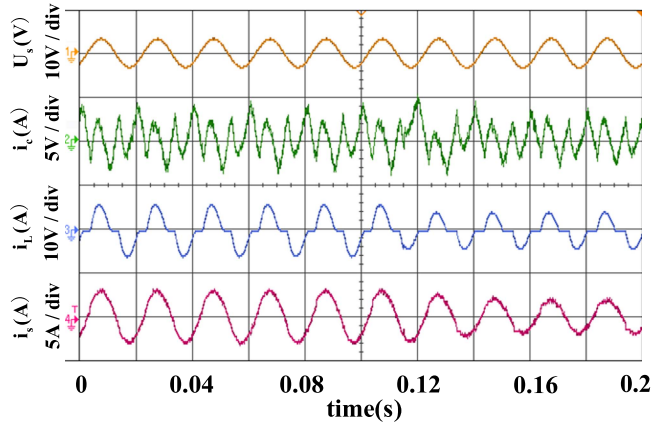

Fig. 37. Dynamic response curve of the comparison method.

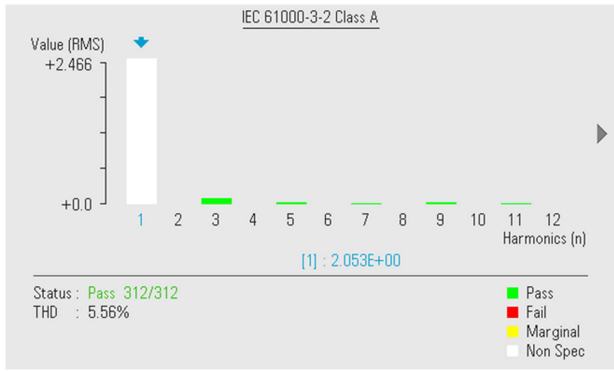

Fig. 38. Power supply current spectrogram after the load increases using comparison method.

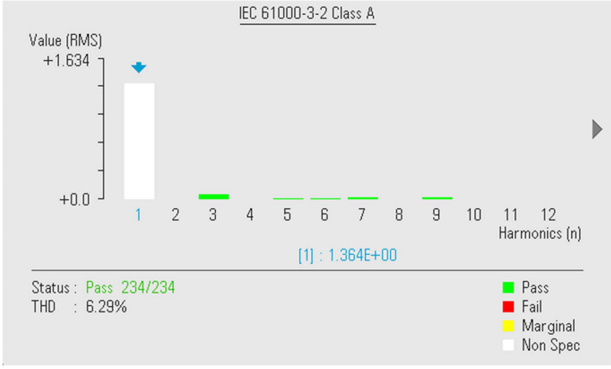

Fig. 39. Power supply current spectrogram after the load decreases using the comparison method.

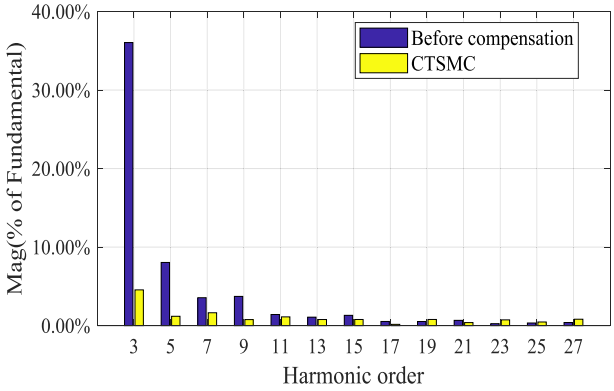

Fig. 40. Comparison of the harmonic content of each order before and after compensation under the CTSMC method.

TABLE VIII
PERFORMANCE INDEX COMPARISON

State / Strategy	Steady state	Load increase	Load decrease
SMC	8.55%	7.36%	9.36%
CTSMC	5.98%	5.56%	6.29%
CTSMC-MLNN	4.24%	3.50%	4.70%

TABLE IX
PERFORMANCE INDEX COMPARISON

State / Strategy	Steady state	Load increase	Load decrease
ASMC-RFNN	6.30%	4.37%	6.74%
DTSMC-DHLRNN	5.90%	5.36%	5.76%
CTSMC-MLNN	4.24%	3.50%	4.70%

both the steady-state response and the dynamic response. A conclusion can be drawn that the intelligent CTSMC method has a stronger ability of harmonics suppression under a smaller sliding-mode gain than SMC and CTSMC methods.

To further demonstrate the superiority of the proposed method, the ASMC using a recurrent fuzzy neural network control method (ASMC-RFNN) and the dynamic terminal sliding-mode control using a double hidden layer recurrent neural network (DTSMC-DHLRNN) are compared [28], [29], as shown in Table IX.

Obviously, compared with the existing DTSMC-DHLRNN method, the THD of the CTSMC-MLNN method is lower by 1.66% at a steady state. Meanwhile, the THD using the CTSMC-MLNN method is 1.86% and 1.06% lower than that of the DTSMC-DHLRNN method under load increases and load decreases, respectively. Meanwhile, compared with ASMC-RFNN, the proposed CTSMC-MLNN still maintains a THD performance improvement of more than about 1%. In summary, the proposed method has better harmonic compensation performance than the two comparison methods.

Furthermore, in order to observe the harmonic suppression effect of different algorithms in the hardware experiment in detail, the comparison diagrams of each harmonic content before and after compensation under steady state are shown in Figs. 40 and 41. Obviously, the CTSMC and CTSMC-MLNN methods can well suppress the third, fifth, and seventh harmonics, which

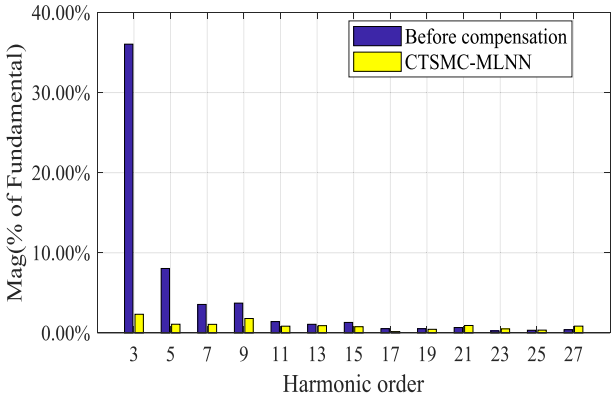

Fig. 41. Comparison of the harmonic content of each order before and after compensation under the CTSMC-MLNN method.

are common and most harmful in the power grid. For the high-frequency harmonic part, in particular, the filtering effect of APF is still obvious even though the harmonics from 13th to 19th are small and less harmful than low-frequency harmonics. However, for the 21st and higher frequency harmonics, the compensation effect designed in this article is not ideal. The relevant reasons are discussed below. Specific data are collected in Table X.

Remark 6: The filtering range of the digital control system of APF is limited by the sampling frequency, the computing power of control equipment, switching frequency, and other factors. The constraint of these factors will cause problems, such as delay in the control link, restriction of system control bandwidth, and unobvious harmonic suppression. Especially for high-frequency harmonics, the above problems are more serious. Therefore, if the filter range of APF is expected to increase, the specification of hardware equipment needs to be improved and the delay in the digital control system needs to be compensated [35].

Remark 7: In practical application, due to the limited compensation ability and capacity of an SAPF, in order to meet the requirements of harmonic control, multiple APFs are often connected to the power grid in parallel. However, there are complex interactions among control loops of APFs. Especially under the condition of a weak power grid, the complex interaction among many large-capacity APF control loops will reduce the stability

TABLE X
COMPARISON OF HARMONIC CONTENT OF EACH ORDER

Order \ Strategy	Before compensation	CTSMC	CTSMC-MLNN
3	34.96%	4.54%	2.32%
5	8.05%	1.18%	1.09%
7	3.62%	1.65%	1.10%
9	3.63%	0.87%	1.08%
11	1.37%	1.12%	0.83%
13	1.12%	0.76%	0.91%
15	1.28%	0.72%	0.74%
17	0.66%	0.18%	0.16%
19	0.58%	0.74%	0.51%
21	0.68%	0.34%	0.79%
23	0.26%	0.75%	0.51%
25	0.34%	0.45%	0.36%
27	0.41%	0.82%	0.52%
THD	36.81%	5.98%	4.24%

of the system, resulting in local instability of the system [36]. Therefore, APF with appropriate capacity can be designed or selected according to the relationship between the short-circuit ratio (SCR) of the grid-connected system and the equivalent impedance of ac system [37].

Remark 8: Actual grid frequencies usually vary within a certain range (49–51 Hz); especially in distributed power networks, frequency fluctuation and offset problems are prominent [6]. This is because in practical applications, there are often long transmission lines and many transformers between the common coupling point and the power supply, resulting in a large equivalent impedance of the grid. Meanwhile, distributed energy is also heavily affected by the environment, resulting in power generation instability, which has a great impact on the harmonic suppression of APF [41]. The CTSMC-MLNN method proposed in this article can also effectively compensate harmonics when grid frequency varies within the range mentioned above due to the strong robustness of CTSMC and the self-learning ability of MLNN. However, the filtering effect is not as good as the simulation and experiment above, especially when the load changes. Therefore, suppression of harmonics in the grid with frequency fluctuations will be investigated for future work.

VII. CONCLUSION

This article proposes a CTSMC strategy combined with MLNN to compensate the harmonic current in the power grid. CTSMC has the characteristics of small tracking error and finite-time convergence. At the same time, the MLNN with good approximation ability and simple structure is used to approximate the unknown nonlinear function in order to reduce the influence of the unmodeled dynamics. The feasibility of the proposed method is verified through detailed simulation and experiments, and the superiority of this method is proved by comparison with other methods. However, the introduction of the NN structure is bound to increase the computational complexity of the algorithm, which will undoubtedly put forward the higher requirements for the computational capacity of the control board in practical applications. The weak grid SCR issue, the impact of frequency variation, and the suppression of harmonics in a grid with frequency fluctuations will be explored in future research

REFERENCES

[1] S. Rahmani, A. Hamadi, K. Al-Haddad, and L. A. Dessaint, "A combination of shunt hybrid power filter and thyristor-controlled reactor for power quality," *IEEE Trans. Ind. Electron.,* vol. 61, no. 5, pp. 2152–2164, May 2014.

[2] X. Sun, R. Han, H. Shen, B. Wang, Z. Lu, and Z. Chen, "A double-resistive active power filter system to attenuate harmonic voltages of a radial power distribution feeder," *IEEE Trans. Power Electron.,* vol. 31, no. 9, pp. 6203–6216, Sep. 2016.

[3] D. Rivas, L. Moran, J. W. Dixon, and J. R. Espinoza, "Improving passive filter compensation performance with active techniques," *IEEE Trans. Ind. Electron.,* vol. 50, no. 1, pp. 161–170, Feb. 2003.

[4] W. U. K. Tareen and S. Mekhielf, "Three-phase transformerless shunt active power filter with reduced switch count for harmonic compensation in grid-connected applications," *IEEE Trans. Power Electron.,* vol. 33, no. 6, pp. 4868–4881, Jun. 2018.

[5] G. Li et al., "A DC hybrid active power filter and its nonlinear unified controller using feedback linearization," *IEEE Trans. Ind. Electron.,* vol. 68, no. 7, pp. 5788–5798, Jul. 2021.

[6] Z.-X. Zou, K. Zhou, Z. Wang, and M. Cheng, "Frequency-adaptive fractional-order repetitive control of shunt active power filters," *IEEE Trans. Ind. Electron.,* vol. 62, no. 3, pp. 1659–1668, Mar. 2015.

[7] D. J. Hogan, F. J. Gonzalez-Espin, J. G. Hayes, G. Lightbody, and R. Foley, "An adaptive digital-control scheme for improved active power filtering under distorted grid conditions," *IEEE Trans. Ind. Electron.,* vol. 65, no. 2, pp. 988–999, Feb. 2018.

[8] J. Fei and L. Liu, "Real-time nonlinear model predictive control of active power filter using self-feedback recurrent fuzzy neural network estimator," *IEEE Trans. Ind. Electron.,* vol. 69, no. 8, pp. 8366–8376, Aug. 2022.

[9] J.-J. Xiong, G.-B. Zhang, J.-X. Wang, and T.-H. Yan, "Improved sliding mode control for finite-time synchronization of nonidentical delayed recurrent neural networks," *IEEE Trans. Neural Netw. Learn. Syst.,* vol. 31, no. 6, pp. 2209–2216, Jun. 2020.

[10] J. Lu, M. Savaghebi, A. M. Y. M. Ghias, X. Hou, and J. M. Guerrero, "A reduced-order generalized proportional integral observer-based resonant super-twisting sliding mode control for grid-connected power converters," *IEEE Trans. Ind. Electron.,* vol. 68, no. 7, pp. 5897–5908, Jul. 2021.

[11] V. Kumar, S. R. Mohanty, and S. Kumar, "Event trigger super twisting sliding mode control for DC micro grid with matched/unmatched disturbance observer," *IEEE Trans. Smart Grid,* vol. 11, no. 5, pp. 3837–3849, Sep. 2020.

[12] J. Baek, M. Jin, and S. Han, "A new adaptive sliding-mode control scheme for application to robot manipulators," *IEEE Trans. Ind. Electron.,* vol. 63, no. 6, pp. 3628–3637, Jun. 2016.

[13] S. Oucheriah and L. Guo, "PWM-based adaptive sliding-mode control for boost DC–DC converters," *IEEE Trans. Ind. Electron.,* vol. 60, no. 8, pp. 3291–3294, Aug. 2013.

[14] J. Li, Q. Zhang, X.-G. Yan, and S. K. Spurgeon, "Observer-based fuzzy integral sliding mode control for nonlinear descriptor systems," *IEEE Trans. Fuzzy Syst.,* vol. 26, no. 5, pp. 2818–2832, Oct. 2018.

[15] F.-J. Lin, P.-H. Chou, C.-S. Chen, and Y.-S. Lin, "DSP-based cross-coupled synchronous control for dual linear motors via intelligent complementary sliding mode control," *IEEE Trans. Ind. Electron.,* vol. 59, no. 2, pp. 1061–1073, Feb. 2012.

[16] J.-P. Su and C.-C. Wang, "Complementary sliding control of non-linear systems," *Int. J. Control,* vol. 75, no. 5, pp. 360–368, Mar. 2002.

[17] Y.-C. Liu, S. Laghrouche, D. Depernet, A. Djerdir, and M. Cirrincione, "Disturbance-observer-based complementary sliding-mode speed control for PMSM drives: A super-twisting sliding-mode observer-based approach," *IEEE J. Emerg. Sel. Topics Power Electron.,* vol. 9, no. 5, pp. 5416–5428, Oct. 2021.

[18] F.-J. Lin, S.-G. Chen, M.-S. Huang, C.-H. Liang, and C.-H. Liao, "Adaptive complementary sliding mode control for synchronous reluctance motor with direct-axis current control," *IEEE Trans. Ind. Electron.,* vol. 69, no. 1, pp. 141–150, Jan. 2022.

[19] F.-J. Lin, J.-C. Hwang, P.-H. Chou, and Y.-C. Hung, "FPGA-based intelligent-complementary sliding-mode control for PMLSM servo-drive system," *IEEE Trans. Power Electron.,* vol. 25, no. 10, pp. 2573–2587, Oct. 2010.

[20] M. Zhou, S. Cheng, Y. Feng, W. Xu, L. Wang, and W. Cai, "Full-order terminal sliding-mode-based sensorless control of induction motor with gain adaptation," *IEEE J. Emerg. Sel. Topics Power Electron.,* vol. 10, no. 2, pp. 1978–1991, Apr. 2022.

[21] H. Hou, X. Yu, L. Xu, K. Rsetam, and Z. Cao, "Finite-time continuous terminal sliding mode control of servo motor systems," *IEEE Trans. Ind. Electron.,* vol. 67, no. 7, pp. 5647–5656, Jul. 2020.

[22] B. Xu, L. Zhang, and W. Ji, "Improved non-singular fast terminal sliding mode control with disturbance observer for PMSM drives," *IEEE Trans. Transp. Electrific.,* vol. 7, no. 4, pp. 2753–2762, Dec. 2021.

[23] S. Dong, M. Liu, Z.-G. Wu, and K. Shi, "Observer-based sliding mode control for Markov jump systems with actuator failures and asynchronous modes," *IEEE Trans. Circuits Syst. II, Express Briefs*, vol. 68, no. 6, pp. 1967–1971, Jun. 2021.

[24] L. Liu and J. Fei, "Extended state observer based interval type-2 fuzzy neural network sliding mode control with its application in active power filter," *IEEE Trans. Power Electron.,* vol. 37, no. 5, pp. 5138–5154, May 2022.

[25] Y. Mi, Y. Song, Y. Fu, and C. Wang, "The adaptive sliding mode reactive power control strategy for wind–diesel power system based on sliding mode observer," *IEEE Trans. Sustain. Energy,* vol. 11, no. 4, pp. 2241–2251, Oct. 2020.

[26] S. Xie and J. Ren, "Recurrent-neural-network-based predictive control of piezo actuators for trajectory tracking," *IEEE/ASME Trans. Mechatronics,* vol. 24, no. 6, pp. 2885–2896, Dec. 2019.

[27] S. C. Yogi, V. K. Tripathi, and L. Behera, "Adaptive integral sliding mode control using fully connected recurrent neural network for position and attitude control of quadrotor," *IEEE Trans Neural Netw. Learn Syst.,* vol. 32, no. 12, pp. 5595–5609, Dec. 2021.

[28] L. Liu, J. Fei, and C. An, "Adaptive sliding mode long short-term memory fuzzy neural control for harmonic suppression," *IEEE Access,* vol. 9, pp. 69724–69734, 2021.

[29] J. Fei and Y. Chen, "Dynamic terminal sliding-mode control for single-phase active power filter using new feedback recurrent neural network," *IEEE Trans. Power Electron.,* vol. 35, no. 9, pp. 9904–9922, Sep. 2020.

[30] L. Zhang, K. Li, H. He, and G. W. Irwin, "A new discrete-continuous algorithm for radial basis function networks construction," *IEEE Trans. Neural Netw. Learn. Syst.,* vol. 24, no. 11, pp. 1785–1798, Nov. 2013.

[31] L. Wuxing, P. W. Tse, Z. Guicai, and S. Tielin, "Classification of gear faults using cumulants and the radial basis function network," *Mech. Syst. Signal Process.*, vol. 18, no. 2, pp. 381–389, 2004.

[32] S.-G. Chen, F.-J. Lin, C.-H. Liang, and C.-H. Liao, "Intelligent maximum power factor searching control using recurrent Chebyshev fuzzy neural network current angle controller for SynRM drive system," *IEEE Trans. Power Electron.*, vol. 36, no. 3, pp. 3496–3511, Mar. 2021.

[33] F.-J. Lin, M.-S. Huang, S.-G. Chen, and C.-W. Hsu, "Intelligent maximum torque per ampere tracking control of synchronous reluctance motor using recurrent Legendre fuzzy neural network," *IEEE Trans. Power Electron.*, vol. 34, no. 12, pp. 12080–12094, Dec. 2019.

[34] F.-J. Lin, C.-I. Chen, G.-D. Xiao, and P.-R. Chen, "Voltage stabilization control for microgrid with asymmetric membership function-based wavelet Petri fuzzy neural network," *IEEE Trans. Smart Grid*, vol. 12, no. 5, pp. 3731–3741, Sep. 2021.

[35] S. Bibian and H. Jin, "Time delay compensation of digital control for DC switchmode power supplies using prediction techniques," *IEEE Trans. Power Electron.,* vol. 15, no. 5, pp. 835–842, Sep. 2000.

[36] P. Dang, T. Ellinger, and J. Petzoldt, "Dynamic interaction analysis of APF systems," *IEEE Trans. Ind. Electron.,* vol. 61, no. 9, pp. 4467–4473, Sep. 2014.

[37] L. Zhang, L. Harnefors, and H.-P. Nee, "Interconnection of two very weak AC systems by VSC-HVDC links using power-synchronization control," *IEEE Trans. Power Electron.,* vol. 26, no. 1, pp. 344–355, Feb. 2011.

[38] J. Fei, Z. Wang, and Q. Pan, "Self-constructing fuzzy neural fractional-order sliding mode control of active power filter," *IEEE Trans. Neural Netw. Learn. Syst.*, to be published, doi: 10.1109/TNNLS.2022.3169518.

[39] J. Fei, Z. Wang, and Y. Fang, "Self-evolving recurrent Chebyshev fuzzy neural sliding mode control for active power filter," *IEEE Trans. Ind. Inform.*, vol. 19, no. 3, pp. 2729–2739, Mar. 2023.

[40] Z. Wang and J. Fei, "Fractional-order terminal sliding-mode control using self-evolving recurrent Chebyshev fuzzy neural network for MEMS gyroscope," *IEEE Trans. Fuzzy Syst.*, vol. 30, no. 7, pp. 2747–2758, Jul. 2022.

[41] H. Lin, X. Guo, D. Chen, S. Wu, and G. Chen, "A frequency adaptive repetitive control for active power filter with 380V/75A SiC-inverter," *IEEE Trans. Ind. Appl.*, vol. 58, no. 4, pp. 5469–5479, Jul./Aug. 2022.